Journal of Materials Chemistry A

Controlling thermoelectric transport via native defects in the diamond-like semiconductors $Cu_2HgGeTe_4$ and Hg_2GeTe_4

Journal:	*Journal of Materials Chemistry A*
Manuscript ID	TA-ART-08-2021-007410.R1
Article Type:	Paper
Date Submitted by the Author:	03-Nov-2021
Complete List of Authors:	Qu, Jiaxing; University of Illinois at Urbana-Champaign, Porter, Claire; Colorado School of Mines Gomes, Lidia; University of Illinois at Urbana-Champaign Adamczyk, Jesse; Colorado School of Mines, Physics Toriyama, Michael; Northwestern University, Materials Science & Engineering Ortiz, Brenden; University of California Santa Barbara, Toberer, Eric; Colorado School of Mines, Ertekin, Elif; University of Illinois, Department of Mechanical Science and Engineering

Journal Name

ARTICLE TYPE

Cite this: DOI: 10.1039/xxxxxxxxxx

Controlling thermoelectric transport via native defects in the diamond-like semiconductors $Cu_2HgGeTe_4$ and Hg_2GeTe_4 †

Jiaxing Qu,[a,*] Claire E. Porter,[b,*] Lídia C. Gomes,[a] Jesse M. Adamczyk,[b] Michael Y. Toriyama,[c] Brenden R. Ortiz,[d] Eric S. Toberer,[b] and Elif Ertekin[a]

Received Date
Accepted Date

DOI: 10.1039/xxxxxxxxxx

www.rsc.org/journalname

Diamond like semiconductors (DLS) have emerged as candidates for thermoelectric energy conversion. Towards understanding and optimizing performance, we present a comprehensive investigation of the electronic properties of two DLS phases, quaternary $Cu_2HgGeTe_4$ and related ordered vacancy compound Hg_2GeTe_4, including thermodynamic stability, defect chemistry, and transport properties. To establish the thermodynamic link between the related but distinct phases, the stability region for both is visualized in chemical potential space. In spite of their similar structure and bonding, we show that the two materials exhibit reciprocal behaviors for dopability. $Cu_2HgGeTe_4$ is degenerately p-type in all environments despite its wide stability region, due to the presence of low-energy acceptor defects V_{Cu} and Cu_{Hg} and is resistant to extrinsic n-type doping. Meanwhile Hg_2GeTe_4 has a narrow stability region and intrinsic behavior due to the relatively high formation energy of native defects, but presents an opportunity for bi-polar doping. While these two compounds have similar structure, bonding, and chemical constituents, the reciprocal nature of their dopability emerges from significant differences in band edge positions. A Brouwer band diagram approach is utilized to visualize the role of native defects on carrier concentrations, dopability, and transport properties. This study elucidates the doping asymmetry between two solid-solution forming DLS phases $Cu_2HgGeTe_4$ and Hg_2GeTe_4 by revealing the defect chemistry of each compound, and suggests design strategies for defect engineering of DLS phases.

1 Introduction

Diamond like semiconductors (DLS) are a chemically diverse family of multinary compounds whose crystallographic structure is based on the diamond prototype. Although several DLS phases like zinc blende GaAs[1–3], chalcopyrite $CuIn_xGa_{1-x}Se_2$ (CIGS)[4–6], and related quaternary Cu_2ZnSnS_4 (CZTS)[7–9] have long been of interest in photovoltaics, their tetrahedral coordination and strong covalent bonding have traditionally been associated with high thermal conductivity, precluding their use as efficient thermoelectric materials. Unexpectedly, many DLS – especially tellurides – have recently been shown to exhibit both high carrier mobilities and low thermal conductivities[10], opening the door to their use in thermoelectric (TE) energy conversion.[10–15] To realize their promise, however, persistent challenges with carrier concentration control must be overcome. In this work, we present a thorough computational and experimental investigation of two promising DLS: quaternary $Cu_2HgGeTe_4$ and related ternary ordered vacancy compound Hg_2GeTe_4, to elucidate the following: (i) the role of native defects on carrier concentrations and transport, (ii) the range of achievable dopability, and (iii) defect engineering strategies that can be applied to other DLS systems to optimize TE performance.

Among the DLS, the I-III-Te_2 chalcopyrites $CuInTe_2$ (CIT) and $CuGaTe_2$ (CGT) were first identified in 2012 as high-performance thermoelectrics due to higher carrier concentrations, high mobility, and moderate lattice thermal conductivity[11–14]. The predicted peak zT is 1.18 at 850 K for CIT[13] and 1.4 at 950 K for CGT[14]. Following this, a computational survey of the Inorganic Crystal Structure Database (ICSD)[16] revealed a group of potentially promising thermoelectrics: quaternary DLS $Cu_2II_BIVTe_4$ (II_B: Zn, Cd, Hg) (IV: Si, Ge, Sn), which exhibit relatively high hole mobilities (> 50 cm^2 V^{-1}s^{-1} at 573 K) alongside exceptionally low lattice thermal conductivity (< 0.25 W m^{-1}K^{-1} at 573 K measured)[10]. Among this group, $Cu_2HgGeTe_4$ shows the highest potential with predicted $zT > 1.5$ at 573 K under optimized doping. The low thermal conductivity of $Cu_2HgGeTe_4$ was at-

---

[*] equal contributions

[a] University of Illinois at Urbana-Champaign, Urbana, IL 61801. [b] Colorado School of Mines, Golden, CO 80401. [c] Northwestern University, Evanston, IL 60208. [d] University of California Santa Barbara, Santa Barbara, CA 93106. E-mail: ertekin@illinois.edu

[†] Electronic Supplementary Information (ESI) available

tributed to both the presence of heavy elements Hg and Te as well as phonon scattering from Cu_{Hg} and Hg_{Cu} antisite defects[10]. While experimentally investigating the $Cu_2HgGeTe_4$ phase diagram, related material Hg_2GeTe_4 was discovered, which exhibits the defect-chalcopyrite structure and forms a full solid solution with $Cu_2HgGeTe_4$[15]. With even lower reported lattice thermal conductivity than $Cu_2HgGeTe_4$[15] and an abundance of vacancy sites in the defect-chalcopyrite structure that can possibly accommodate extrinsic dopants, Hg_2GeTe_4 is also a promising TE candidate. The anomalously low lattice thermal conductivity in Hg_2GeTe_4 can likely be partially attributed to the anharmonicity created by non-bonding Te electrons interacting with adjacent atoms, analogous to the effect of Sb lone pair electrons of in the well-studied Cu-Sb-Se system by Skoug et al.[17]

With low thermal conductivities in place, further improvements to the efficiency of $Cu_2HgGeTe_4$ and Hg_2GeTe_4 require control of carrier concentration to optimize electronic properties. The chemical complexity of both materials presents some challenges in this endeavor, including the high-dimensional chemical phase space, abundance of possible native defects, and large number of secondary phases. The crystal structures of Hg_2GeTe_4 and $Cu_2HgGeTe_4$ are shown in Figure 1. $Cu_2HgGeTe_4$ crystallizes in the stannite structure (space group I-42m) while Hg_2GeTe_4 crystallizes in defect chalcopyrite structure (space group I-4). In stannite $Cu_2HgGeTe_4$, each anion (Te atom) is tetrahedrally coordinated by four cations (two Cu in the nominal valence +1, one Hg in +2, and one Ge in +4). In Hg_2GeTe_4, each anion coordinates with only three cations, resulting in a lone pair of Te electrons. Hg_2GeTe_4 can be derived from $Cu_2HgGeTe_4$ by replacing one Cu atom with one Hg atom and removing another Cu atom, envisioned as the simultaneous creation of one Cu_{Hg} defect and one V_{Cu} defect. The thermoelectric performance descriptor β[18] suggests that both $Cu_2HgGeTe_4$ and Hg_2GeTe_4 could have even better n-type TE performance than PbTe if they could be doped to optimal electron concentrations. However, it is well-known that many DLS materials suffer from doping asymmetry[19,20]. While they often natively exhibit p-type carriers or can readily be doped p-type

In this work, we present a comprehensive analysis of the thermodynamics, defects, and electronic properties of $Cu_2HgGeTe_4$ and Hg_2GeTe_4. Both materials' stability are determined by density functional theory (DFT) and visualized together in chemical potential space. DFT predictions for phase competition are validated using experimental phase boundary mapping. Calculations of native carrier concentrations and effective mass values are supported by electronic transport measurements. The defect calculations reveal the boundaries of achievable carrier concentrations for both compounds if suitable extrinsic dopants can be identified. $Cu_2HgGeTe_4$ is found to be degenerately p-type in all thermodynamic environments despite its wide stability window, while Hg_2GeTe_4 shows both p- and n-type dopability windows in spite of its narrower stability region and intrinsic character. An understanding of the defect chemistry in $Cu_2HgGeTe_4$, Hg_2GeTe_4, and the interplay between the two (Cu-doped Hg_2GeTe_4) gives insight into the doping asymmetry in DLS phases and offers possible strategies to overcome this doping challenge.

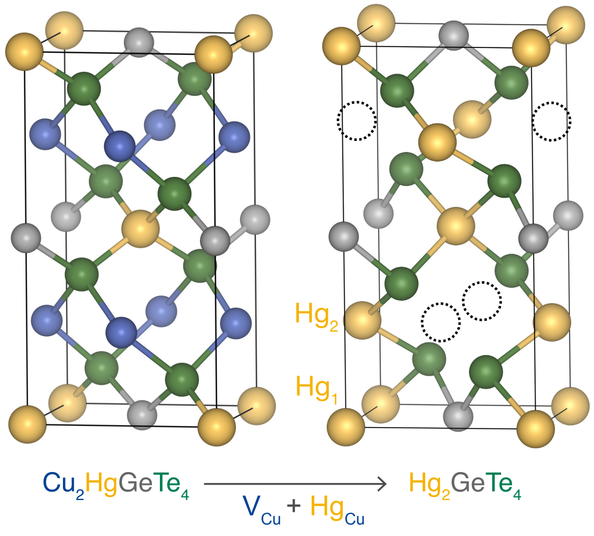

Fig. 1 $Cu_2HgGeTe_4$ crystallizes in the stannite structure, while Hg_2GeTe_4 adopts the defect chalcopyrite structure. Transitions from the quaternary to the ternary structure (which form a full solid solution) may be understood as the simultaneous substitution of one Hg atom onto a Cu site and the creation of a Cu vacancy.

2 Results and discussion

2.1 Phase stability analysis

We begin by determining the stability regions for $Cu_2HgGeTe_4$ and Hg_2GeTe_4. Phase stability analysis (see Section 4.2) provides information about the range of thermodynamic environments under which a compound is stable. Thermodynamic environments are described by a set of chemical potentials $\Delta\mu_i(T,P)$. For each element i, $\Delta\mu_i$ indicates its availability, with more negative values indicating that the element is relatively poor (and less negative values indicating that it is rich) in the environment. At a given temperature T and pressure P, a compound is stable for only a well-defined range of chemical potentials. Outside this range, decomposition to other secondary phases occurs. A ternary compound may be stable as a single phase, two-phase, or three-phase equilibrium while a quaternary compound can be stable in a single, two, three, or four-phase equilibrium. In general, when an n-element compound is in equilibrium with n phases (including itself), the corresponding set of $\Delta\mu_i$ are fixed (invariant points). Critically, controlling chemical potentials during growth provides an opportunity to tune defect concentrations to obtain control over carriers (their type and quantity), dopability, and transport.

The four-dimensional chemical potential space spanned by $\Delta\mu_{Cu}$–$\Delta\mu_{Hg}$–$\Delta\mu_{Ge}$–$\Delta\mu_{Te}$ contains the stability region where $Cu_2HgGeTe_4$ is thermodynamically stable ($2\Delta\mu_{Cu} + \Delta\mu_{Hg} + \Delta\mu_{Ge} + 4\Delta\mu_{Te} = \Delta H_{CHGT}$); this region is a filled 3D polyhedron. Figures 2a and b show this polyhedron in 3D by projecting along the $\Delta\mu_{Te}$ axis. The $\Delta\mu_{Te}$ axis was chosen for projection because, as we will show, Te-related defects are so energetically costly that displaying the remaining Cu, Ge, and Hg axes renders more use-

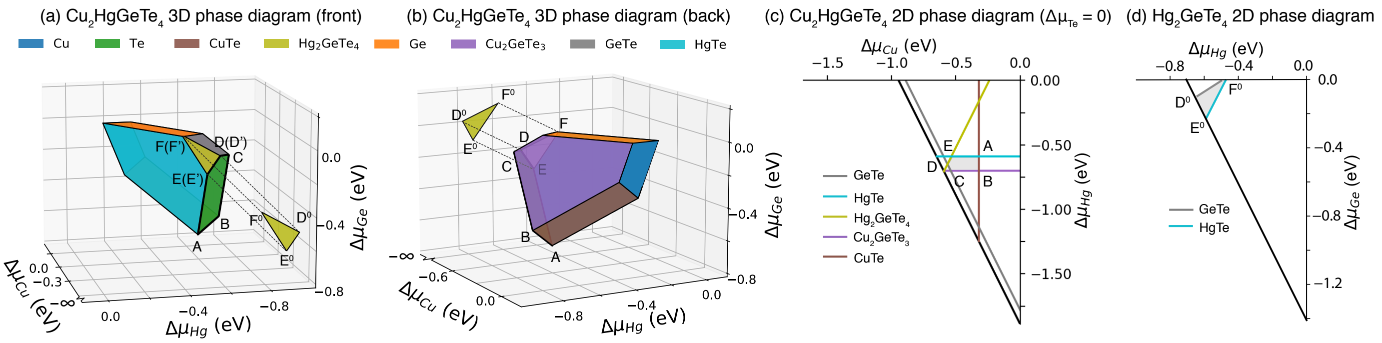

Fig. 2 Front view (a) and back view (b) of the stability region of Cu$_2$HgGeTe$_4$ which forms a polyhedron in the three-dimensional chemical potential space. The color index represents different secondary phases. The two-dimensional projection of the stability region on the $\Delta\mu_{Cu}$ and $\Delta\mu_{Hg}$ plane is shown by the grey-shaded area in (c) at Te-rich condition. Points A and B correspond to Cu-rich and Cu-poor growth conditions respectively. Stability region for Hg$_2$GeTe$_4$ (d) on the $\Delta\mu_{Hg}$ and $\Delta\mu_{Ge}$ plane, bound by points D^0, E^0, F^0.

ful and interesting information. Each point inside the polyhedron corresponds to a set of chemical potentials for which Cu$_2$HgGeTe$_4$ is stable. Each colored face of the polyhedron represents a two-phase equilibrium of Cu$_2$HgGeTe$_4$ with a secondary compound, thereby putting a restriction on the available set of chemical potentials of the quaternary compound. Likewise, the edges of the polyhedron represent domains of three-phase equilibrium while vertices indicate four-phase equilibrium. Vertices correspond to invariant points, the points of fixed chemical potentials. In total, we find 12 invariant points representing 12 distinct four-phase equilibria, in good agreement with our prior experimental phase boundary mapping of Cu$_2$HgGeTe$_4$ [15] which identified 13. One experimentally detected phase Cu$_{1.4}$Te is missing in our calculations, as the structure is unknown has not yet been characterized. The stability region of Cu$_2$HgGeTe$_4$ spans a large range of chemical potentials for Cu (0.56 eV), Hg (0.53 eV), Ge (0.66 eV), and Te (0.43 eV). Such differences in atomic chemical potentials ($\Delta\mu_i$) for host elements results in distinct defect energies at different growth conditions, allowing tunability of the carrier concentration.

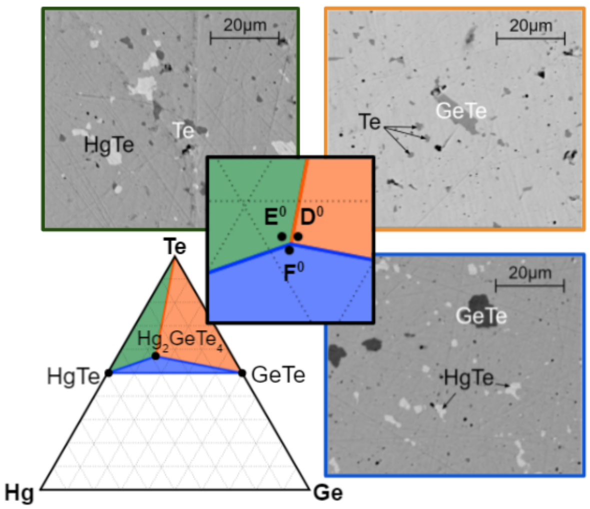

Fig. 3 Phase stability region of Hg$_2$GeTe$_4$ in composition space with SEM images of samples at different growth conditions. E^0, D^0, and F^0 match the same labels in Figure 2(d).

We will subsequently show that both Te- and Ge-related defects have relatively high energy for all equilibrium chemical potentials; as such, we can further project the polyhedron of Fig 2a,b to the $\Delta\mu_{Cu}$-$\Delta\mu_{Hg}$ plane. In Figure 2c, we have invoked that Cu$_2$HgGeTe$_4$ is in equilibrium with elemental Te ($\Delta\mu_{Te} = 0$) which selects the A-B-C-D-E plane in green from the polyhedron when the projection is made. At the Te-rich condition (plane A-B-C-D-E), the secondary binary and ternary phases that are in equilibrium with Cu$_2$HgGeTe$_4$ include: CuTe (*Pmmn*, orthorhombic), GeTe (*R3m*, trigonal), HgTe ($F\bar{4}3m$, cubic), Cu$_2$GeTe$_3$ (*Imm2*, orthorhombic) and Hg$_2$GeTe$_4$ ($I\bar{4}$, tetragonal), which confirms previous experimental observations [15].

The shape of the stability region of Cu$_2$HgGeTe$_4$ is similar to that of Cu$_2$ZnSnS$_4$ (CZTS) [21,22] and Cu$_2$ZnSnSe$_4$ (CZTSe) [22] due to the similar chemical composition and secondary phases. Too much Hg (higher $\Delta\mu_{Hg}$) leads to HgTe formation while too little Hg (lower $\Delta\mu_{Hg}$) leads to Cu$_2$GeTe$_3$ formation. At the most Cu-rich growth conditions (points A, B in Figure 2c), Cu$_2$HgGeTe$_4$ is in equilibrium with CuTe, Te, and HgTe or Cu$_2$GeTe$_3$, respectively. At the most Cu-poor growth condition (point D), Cu$_2$HgGeTe$_4$ is in equilibrium with Te, Hg$_2$GeTe$_4$, and GeTe. It is worth noting that previous experimental work found that Hg$_2$GeTe$_4$ and Cu$_2$HgGeTe$_4$ share a full solid solution [15], while first-principles calculations show phase segregation of Hg$_2$GeTe$_4$ and Cu$_2$HgGeTe$_4$ into separate distinguishable phases that are in equilibrium with each other (point D, E, and F in Figure 2). From our previous modeling of disordered configurations for intermediate alloy compositions [23], the mixing enthalpy lies below 10 meV/atom, indicating that there is no strong preference for phase segregation, and the formation of solid solutions is expected at finite temperatures above 0 K due to the stabilizing contribution of mixing entropy. Our first-principles based phase stability calculations are performed at 0 K without entropy contributions while experimental synthesis and measurements are performed at T = 623 K and T > 323 K, respectively. Including temperature dependent contributions even at modest temperatures would reproduce the experimental observation that Hg$_2$GeTe$_4$ and Cu$_2$HgGeTe$_4$

form a solid solution.

The stability region of pure Hg_2GeTe_4 is also shown in Figure 2a and b. In the three-dimensional space formed by $\Delta\mu_{Cu}$, $\Delta\mu_{Hg}$, and $\Delta\mu_{Ge}$, the stability region of pure Hg_2GeTe_4 is located at the maximally Cu deficient growth condition (plane $\Delta\mu_{Cu} = -\infty$). On this plane, the stability region of Hg_2GeTe_4 is denoted by the triangular plane D^0-E^0-F^0. Meanwhile plane D-E-F represents the equilibrium between $Cu_2HgGeTe_4$ and Hg_2GeTe_4; it corresponds to Hg_2GeTe_4 with some amount of Cu dissolved in. Since pure Hg_2GeTe_4 does not depend on $\Delta\mu_{Cu}$, the stability region of Hg_2GeTe_4 is bounded by plane D-E-F on one side and must continue along the $\Delta\mu_{Cu}$ axis as $\Delta\mu_{Cu} \to -\infty$. As such, we can conclude that the full stability region is the projection to the front surface ($\Delta\mu_{Hg}$, $\Delta\mu_{Ge}$) of Figure 2a. The solid volume demarcated by the dashed lines connecting planes D-E-F and D^0-E^0-F^0 shows the stability region of Hg_2GeTe_4 containing different amounts of dissolved Cu into the ordered vacancy lattice.

The phase boundaries of pure Hg_2GeTe_4 can also be projected into two dimensions along the $\Delta\mu_{Te}$ axis to the plane spanned by $\Delta\mu_{Hg}$ and $\Delta\mu_{Ge}$, as shown in Figure 2d. The relatively narrow stability region indicates that the chemical potentials for host elements Hg, Ge and Te do not vary significantly in different parts of the stability region. In contrast to the large stability region for $Cu_2HgGeTe_4$, Hg_2GeTe_4 is stable across a narrow set of chemical potentials which will ultimately limit the ability to tune native defects synthetically.

We conclude our tour of the phase stability regions of both compounds with a note on the shape of the computed phase stability region of Hg_2GeTe_4 (Figure 2d). This 2D region is shown as a triangle (with vertices D^0, E^0, and F^0) but the ternary phase stability region is actually bounded by 4 vertices (representing three-phase equilibrium) two of which are nearly coincident. From computation we found that Hg_2GeTe_4 can be in equilibrium with binary phases GeTe ($R3m$, trigonal) and HgTe ($F\bar{4}3m$, cubic) as well as with elemental phases of Ge and Te. Point F^0 actually consists of two different vertices that are very close to each other (0.05 eV difference in $\Delta\mu_{Hg}$), corresponding to the equilibria of *HgTe*-Ge-Hg_2GeTe_4 and of *GeTe*-Ge-Hg_2GeTe_4. Close inspection of Figure 2d along the $\Delta\mu_{Hg}$ axis reveals this small gap between where GeTe and HgTe appear to intersect. From experiment we do not observe three-phase equilibrium with elemental Ge. Instead of Ge, our experiments reveal a phase coexistence of HgTe-*GeTe*-Hg_2GeTe_4, which is represented by point F^0 (at the intersection of phase lines GeTe and HgTe). This discrepancy between DFT and experiment arises from uncertainties in DFT-computed relative energies, and would be resolved if the the formation enthalpy of Hg_2GeTe_4 in DFT was reduced by only 0.05 eV per unit cell.

To unite theory and experiment, samples were prepared under synthetic control of chemical potentials via phase-boundary mapping (PBM)[24], which is an experimental technique that leverages the presence of intentional trace impurity phases to determine the native chemical potentials within the sample. Just as the vertices in Figures 2a-b represent invariant points of fixed chemical potentials in the quaternary system, the vertices in Figure 2d represent invariant points in the ternary system (where three compounds are in equilibrium instead of four). The PBM of $Cu_2HgGeTe_4$ has already been reported[15]; the PBM of Hg_2GeTe_4 in composition space is shown in Figure 3 together with SEM images of samples at different corners of the phase stability region. For example, preparation of a multi-phase sample that includes predominantly Hg_2GeTe_4 but with trace impurities of Te and HgTe (confirmed through SEM) fixes the chemical potentials at vertex E^0. The area that represents three-phase equilibrium for Hg_2GeTe_4 with Te and HgTe (or Te and GeTe, or HgTe and GeTe) in composition space corresponds to a single point in chemical potential space. Therefore, the green, orange, and blue regions in Figure 3 match vertices E^0, D^0 and F^0 in Figure 2d respectively.

This comprehensive phase stability analysis for $Cu_2HgGeTe_4$ and Hg_2GeTe_4 maps out their stability region in chemical potential space and will provide guidance for synthetic control of chemical potentials. We can achieve specific chemical potentials by controlling growth conditions to yield samples with specific equilibrium trace impurities, pinning them to specific invariant points in chemical potential space to achieve desirable carrier concentrations.

2.2 Defect chemistry

With an understanding of the phase stability, it is now possible to predict the achievable dopability range in both $Cu_2HgGeTe_4$ and Hg_2GeTe_4 using defect chemistry. The dopability of each compound is established by considering the types of native defects that are present, and their concentrations, at each invariant point in chemical potential space. By considering the defect formation energies at each invariant point, we can determine the equilibrium defect concentrations, the corresponding n-type and p-type free carrier concentrations, and the effective Fermi energy (see Section 4.4). Importantly, the invariant points represent extremal values of chemical potential space for which the compound is stable (*e.g.* Cu-rich to Cu-poor). By considering defect chemistry at all invariant points, the achievable dopability at different growth conditions for a compound can be established. As we will describe below, predicted carrier concentrations can also be directly compared to experimental measurements via phase boundary mapping.

$Cu_2HgGeTe_4$: The formation energies of native point defects for $Cu_2HgGeTe_4$ as a function of the Fermi energy (E_F) are shown in Figure 4a,b. The native defects considered include vacancies (V_{Cu}, V_{Hg}, V_{Ge}, V_{Te}), antisite defects (Ge_{Hg}, Hg_{Ge}, Cu_{Hg}, Hg_{Cu}) and self-interstitials (Cu_i), all of which are considered in varying charge states. For each defect type, we follow the convention that only the minimum energy charge state is shown. Here, Cu_i defects sits on the tetrahedral site (Figure S9). Note that Figure 2a shows the formation energies of defects at point B, which represents the four-phase equilibrium between Te-Cu_2GeTe_3-CuTe-$Cu_2HgGeTe_4$. The panel on the right shows the defect energies at point F, the four-phase equilibrium between HgTe-Hg_2GeTe_4-GeTe-$Cu_2HgGeTe_4$. Compared to each other, point B represents a relatively Cu-rich environment, and point F a relatively Cu-poor environment.

Under both Cu-rich and Cu-poor conditions, we observe that cation vacancies V_{Cu} and V_{Hg}, as well as the antisite defect Cu_{Hg}, are the primary acceptor defects in $Cu_2HgGeTe_4$, while antisite Hg_{Cu} is the lowest-energy donor defect. Since both the acceptor vacancy V_{Cu} and acceptor antisite Cu_{Hg} have ultra-low formation energies compared to the donor Hg_{Cu} in all cases, $Cu_2HgGeTe_4$ is found to exhibit degenerately p-type conductivity across all the invariant points on A-B-C-D-E green plane. In both the Cu-poor and Cu-rich cases, the effective Fermi energy E_F^{eff} (Section 4.4) lies inside the valence bands. At the Cu-rich growth condition (Figure 4a), the antisite defect Cu_{Hg} has negative defect formation energy for all Fermi energies within the band gap, ensuring that E_F^{eff} lies well below the valence band edge. The $\Delta E_{D,q}$ for neutral Cu_{Hg} antisite defect is 0.047 and 0.0431 eV at Cu-rich (B) and Cu-poor (F) conditions, resulting in charge transition levels $Cu_{Hg}(0|-1)$ that are 0.255 and 0.246 eV below the VBM. Attempts to dope the material n-type by mitigating Cu_{Hg} via choosing a more Cu-poor environment are foiled by the subsequent drop in energy of V_{Cu}. These two defects ensure degenerately p-type carrier concentrations across the entire A-B-C-D-E green plane (and, in fact, the whole stability region of the quaternary).

Cu-related antisite defects Cu_{Hg} and Hg_{Cu} are predominant through the whole Fermi energy range. High-temperature X-ray diffraction[10] has confirmed the existence of these two antisite defects. The favorability of these defects can be understood by the energetic proximity of the stannite and kesterite phases[25–28], which differ from each other only by the arrangement of the group I_B and II_B cations. The antisite defects Hg_{Cu} and Cu_{Hg} likely contribute to anomalously low κ_L (< 0.25 W $m^{-1}K^{-1}$ at 573 K measured) in $Cu_2HgGeTe_4$ because they introduce disorder into the lattice periodicity and contribute to point defect scattering of phonons. This is believed to be a contributing factor to $Cu_2HgGeTe_4$'s ultra-low κ_L in experiment.

Another predominantly low-energy defect is V_{Cu}, which is notoriously common in Cu-based semiconductors and often associated with p-type electrical transport.[4,29–33] Attempts to suppress the formation of V_{Cu} through off-stoichiometric synthesis at Cu-rich growth conditions (Figure 4a) will simply increase the Cu_{Hg} concentration. These low-energy native defects make n-type doping of $Cu_2HgGeTe_4$ through extrinsic elements challenging, and lead us to conclude that it will be difficult, if not impossible, to synthesize $Cu_2HgGeTe_4$ with electrons as the majority carrier.

Like many other DLS materials, the n-type TE potential of $Cu_2HgGeTe_4$ will surpass that of p-type if it can be doped to the optimal carrier concentration.[10,15,18,19] Although the n-type TE performance of $Cu_2HgGeTe_4$ is predicted to be four times better than PbTe according to the TE material descriptor β[15], we find that the n-type dopability is restricted by low-energy Cu-related acceptor defects that resist extrinsic doping. From a design perspective, a Cu-free analog to $Cu_2HgGeTe_4$ may help open up the dopability window, which is demonstrated by our following defect calculations on Hg_2GeTe_4.

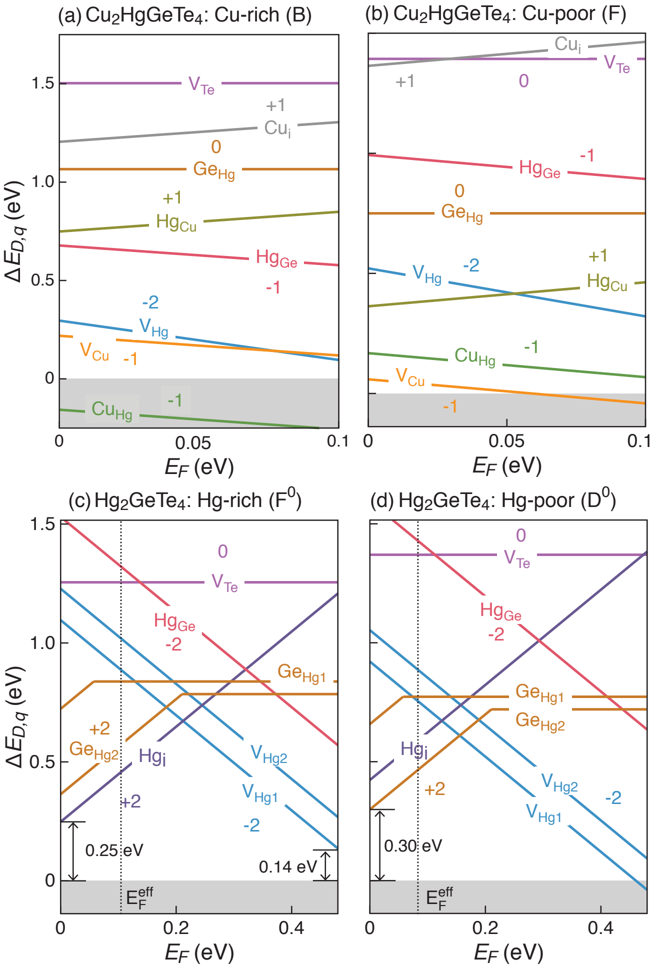

Fig. 4 Defect formation energy for native point defects as a function of Fermi energy (E_F) in $Cu_2HgGeTe_4$ under (a) Cu-rich and (b) Cu-poor conditions, calculated using the HSE06 functional and band edge shifts from HSE06+SOC. Cu interstitials are placed in the tetrahedral interstitial site. Defect formation energy for native point defects as a function of Fermi energy in Hg_2GeTe_4 under (c) Hg-rich and (d) Hg-poor conditions, calculated using the HSE06 functional and band edge shifts from HSE06+SOC. Hg interstitials are placed in the vacancy site. The effective Fermi energy is shown by the dashed vertical line, which is the position of Fermi energy when the system is quenched from the synthesis temperature. For Hg_2GeTe_4, the positive energy windows ΔE_{don} of 0.14 eV and ΔE_{acc} of 0.25 eV are favorable for p- and n-type extrinsic doping.

Hg_2GeTe_4: Figure 4c,d show the defect formation energies as a function of the Fermi energy for six different native defects (V_{Hg}, V_{Ge}, V_{Te}, Ge_{Hg}, Hg_{Ge}, Hg_i) in Hg_2GeTe_4, at points F^0 and D^0 in Figure 2 corresponding to Hg-rich (c) and Hg-poor (d) growth conditions, respectively. Here, the interstitial site refers to the 'vacant' site of the ordered vacancy compound previously occupied by half of the Cu atoms in $Cu_2HgGeTe_4$ (Figure 1). The other Cu sites in $Cu_2HgGeTe_4$ are now occupied by Hg atoms, forming a distinct Wyckoff position from the original Hg atoms. As such, we consider both of the inequivalent Hg sites for V_{Hg} and Ge_{Hg} defects. Due to the narrow stability window, the defect chemistry does not vary significantly under different growth conditions. In contrast to $Cu_2HgGeTe_4$, Hg_2GeTe_4 is predicted to exhibit a more intrinsic character, with the effective Fermi energy (E_F^{eff}) residing between mid-gap and the VBM under both Hg-rich and Hg-poor conditions. The most favorable defects in Hg_2GeTe_4 (V_{Hg}, Ge_{Hg}, and Hg_i) have comparably higher energies than the most favorable defects in $Cu_2HgGeTe_4$.

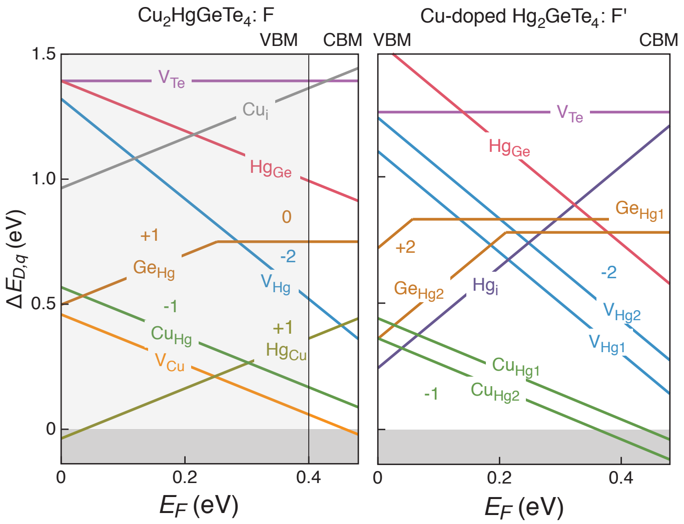

Fig. 5 Comparison of defect chemistry for Cu-doped Hg_2GeTe_4 and $Cu_2HgGeTe_4$ at the same set of chemical potentials. The energy domain for $Cu_2HgGeTe_4$ has been widened to reproduce the band gap for Hg_2GeTe_4 (ΔE_{VBM} = -0.38 eV). The shift of valence band is shaded in grey for $Cu_2HgGeTe_4$. To facilitate comparison, defects that correspond to each other are shown in the same color for both materials.

It is interesting to note that Hg_2GeTe_4 has a wider predicted band gap than $Cu_2HgGeTe_4$: 0.48 eV in comparison to 0.10 eV. By removing the Cu from $Cu_2HgGeTe_4$, the electronic states contributed by Cu d-orbitals at the top of valence bands of $Cu_2HgGeTe_4$ (Figure S3) are also removed, opening up the band gap of Hg_2GeTe_4. Cu d-orbitals are known to hybridize with p-orbitals of Group VI atoms in other Cu-containing DLS compounds and contribute to small or even pseudo-gaps[34]. Also, by removing Cu constituents, the dominant Cu-containing defects (Cu_{Hg}, Hg_{Cu} and V_{Cu}) in $Cu_2HgGeTe_4$ are now no longer present, and the remaining native defects possess relatively high formation energies, leaving behind an intrinsic character and a dopability window for Hg_2GeTe_4. The positive energy windows ΔE_{don} of 0.14 eV and ΔE_{acc} of 0.25 eV are favorable for low-energy donor dopants and acceptor dopants. A donor/acceptor dopant with formation enthalpy lower than the respective energy window will dope Hg_2GeTe_4 n- or p-type, without forming compensating native defects. As such, the doping efficiency could be high if the growth conditions were well-chosen and a suitable extrinsic dopant was found.

Hg_2GeTe_4 with Cu present: So far we have considered the defect chemistry of Hg_2GeTe_4 in an environment that has no Cu present (plane D^0-E^0-F^0, located at $\Delta\mu_{Cu} = -\infty$). Since we are interested in understanding the relationship between the defect chemistry of $Cu_2HgGeTe_4$ and Hg_2GeTe_4 it is valuable to also consider the defect chemistry of Hg_2GeTe_4 when Cu is present and can be incorporated as an extrinsic p-type dopant. To explore this, we consider the defect chemistry of Hg_2GeTe_4 on plane D'-E'-F' (Figure 2), which are three growth conditions when all the Cu-containing secondary phases are considered in the Cu-Hg-Ge-Te chemical space. Vertices D, E, and F of $Cu_2HgGeTe_4$ and D', E', and F' of Cu-doped Hg_2GeTe_4 have identical chemical potential sets due to the intersection of the two (hyper) planes created by their thermodynamic equilibrium equations.

To explain the relationship between $Cu_2HgGeTe_4$ and Hg_2GeTe_4, Figure 5 compares the defect formation energy diagrams at F' and F, where the two materials have the same set of chemical potentials. For Hg_2GeTe_4 the diagram shows that Cu is an effective extrinsic p-type dopant due to the low-energy Cu_{Hg} defect, which is analogous to the corresponding antisite defect in $Cu_2HgGeTe_4$. We found that the Cu_{Hg2} antisite defects have lower $\Delta E(D,q)$ than Cu_{Hg1}, indicating that Cu replacement on site 2 Hg (Figure 1) is more favorable. This conclusion is in agreement with a theoretical and experimental work on Cu incorporation into the $Cu_{2x}Hg_{2-x}GeTe_4$ alloy structure which reveals that the incorporation of Cu occurs preferentially on site 2 planes before filling the other planes.[23]

In Figure 5, the Fermi energy domain shown for $Cu_2HgGeTe_4$ is widened to match the band gap of Hg_2GeTe_4, and the diagrams are aligned via their conduction band edges. Interestingly, a correspondence of the defect chemistries of the two materials is found. For most native defects, the favorable charge states, defect formation energies and charge transition levels (CTL) are preserved between Cu-doped Hg_2GeTe_4 and $Cu_2HgGeTe_4$. For instance, low-energy acceptor defects Cu_{Hg} and V_{Hg} have almost the same defect formation energies in the two compounds. The CTL for Ge_{Hg} near mid-gap is also recovered in the extended energy window of $Cu_2HgGeTe_4$. Despite the difference in crystal structures, the high similarity between the defect chemistries of Cu-doped Hg_2GeTe_4 and $Cu_2HgGeTe_4$ reveals that the locally-preserved tetrahedral bonding is a governing factor in determining defect formation energies.

2.3 Transport properties

Despite their chemical and structural similarities, the transport properties of $Cu_2HgGeTe_4$ and Hg_2GeTe_4 are quite different. In the following, we present a Brouwer band diagram inspired approach (Figure 6) to plot carrier/defect concentrations, ideal dopability (defined in Section 2.3.3), and Seebeck coefficient along the relevant chemical potential paths. The chemical potential path travels from Cu-rich to Cu-poor conditions, passing through three distinct regions: $Cu_2HgGeTe_4$ (A to F), Cu-doped Hg_2GeTe_4 (D' to F'), and Cu-free Hg_2GeTe_4 (D^0 to F^0) (Figure 2).

2.3.1 Defect and carrier concentrations

In Figure 6a, the native free carrier concentrations at T = 50° are shown together with defect concentrations along the chemical potential path, including comparison with computational results (lines) and experimental measurements (symbols). See the temperature dependent measured and predicted carrier concentrations in Figure S10. The carrier and defect concentrations are calculated following a 'quench' picture, in which the total concentration of each type of defect is fixed at the synthesis temperature while the relative concentrations of all charge states of a given defect equilibrate with the measurement temperature (Section 4.4). The experimental carrier concentrations are measured using phase-boundary mapping. In general, the predicted carrier con-

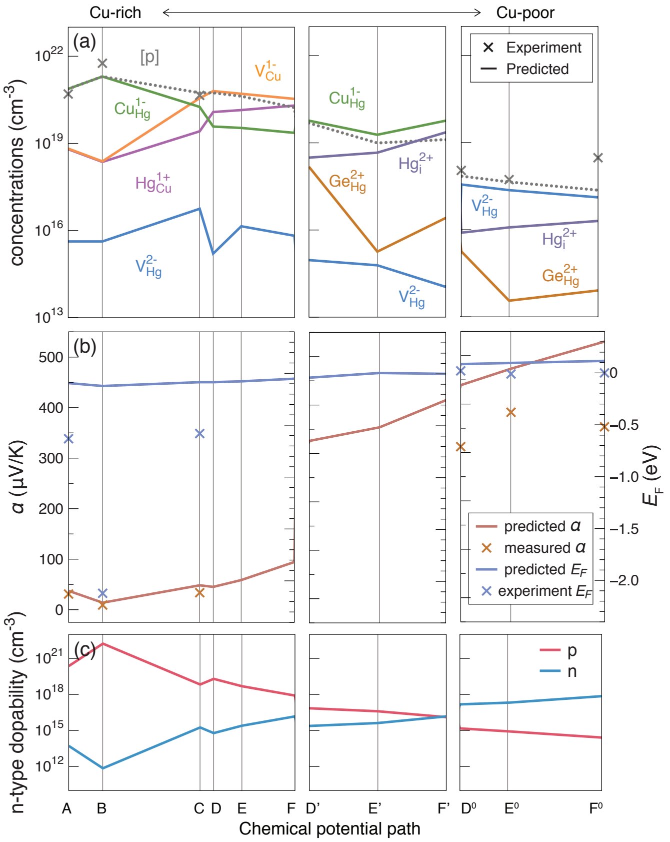

Fig. 6 Brouwer band diagram of transport properties plotted along the chemical potential path from $Cu_2HgGeTe_4$ to Hg_2GeTe_4 at T = 50°. (a) Defect concentrations (solid lines) and carrier concentrations (dashed lines) from first-principles defect calculations and experiment Hall measurements (x symbols). (b) Seebeck coefficient (α) shown together with position of Fermi energy (E_F) reference to VBM for that material. (c) ideal n-type dopability represented by maximum achievable electron concentrations, with labels for both electron (blue) and hole (red) concentrations.

centrations (dashed lines) at 323 K are in good agreement with experimental Hall measurements, within one order of magnitude for Hg_2GeTe_4 and even better for $Cu_2HgGeTe_4$. No experimental data are provided for the middle panel in Figure 6 due to the formation of a solid-solution between $Cu_2HgGeTe_4$ and Hg_2GeTe_4.

The predicted hole concentrations for $Cu_2HgGeTe_4$ (A to F) range from 1.7×10^{20} to 2.0×10^{21} cm^{-3}, spanning one order of magnitude along the chemical potential path. It is apparent that the high native carrier concentrations arise from the two low-energy defects previously identified, Cu_{Hg} for more Cu-rich conditions and V_{Cu} for more Cu-poor conditions. Therefore, attempts to suppress the formation of one defect (e.g. Cu_{Hg}) will facilitate the formation of the other (e.g. V_{Cu}), resulting in the degenerate p-type character of $Cu_2HgGeTe_4$ for all growth conditions.

The middle panel of 6a shows Cu-doped Hg_2GeTe_4, where Cu-related defects are limited to Cu_{Hg} antisite defects. The defect chemistry of Cu-doped Hg_2GeTe_4 is distinct from that of $Cu_2HgGeTe_4$ due to the absence of V_{Cu} defects, leaving Cu_{Hg} as the only dominant defect. This negatively charged defect achieves charge neutrality by creating holes, resulting in a p-type character for Cu-doped Hg_2GeTe_4. The predicted hole concentrations for this doped compound bridge the gap between degenerately p-type $Cu_2HgGeTe_4$ and intrinsic Hg_2GeTe_4, ranging from 9.9×10^{18} to 4.8×10^{19} cm^{-3}. Aside from the dominant defect Cu_{Hg}, Ge_{Hg} and Hg_i also manifest in high concentrations, while V_{Hg} appears in lower concentrations.

Finally, we consider the defects and carriers of Cu-free Hg_2GeTe_4, shown on the rightmost side of Figure 6a. At Cu-deficient ($\Delta\mu_{Cu} = -\infty$) conditions where Hg_2GeTe_4 is stable (plane D^0-E^0-F^0 in Figure 2), the native carrier concentrations are largely set by dominant defect V_{Hg}, with predicted hole concentrations ranging from 2.0×10^{17} to 7.0×10^{17} cm^{-3}. The theoretical carrier concentrations somewhat underestimate experiment, which may arise from an overestimated band gap. Conversely, the experimental carrier concentration could be high due to the presence of trace impurities or unintentional dopants.

2.3.2 Seebeck coefficients, Fermi energy, and effective masses

Seebeck coefficient (α) calculations were performed using AMSET[35], with input carrier concentrations (to account for ionized impurity scattering) from first-principles defect calculations at 323 K. Experimental Seebeck coefficients were measured in-house on a custom instrument[36] (see Section 4.7). These are compared in Figure 6b. No experimental data are shown for D, E, F, D', E', or F' due to the formation of an alloy between $Cu_2HgGeTe_4$ and Hg_2GeTe_4[15]. The computed and measured Seebeck coefficients are in very good agreement for $Cu_2HgGeTe_4$, which is not surprising due to its high carrier concentration to which the Seebeck coefficient is only weakly sensitive. $Cu_2HgGeTe_4$ exhibits metallic behavior for its Seebeck coefficient, consistent with a degenerate semiconductor (<35 μV/K). Conversely, measured α values for Hg_2GeTe_4 are significantly higher (300 to 400 μV/K) and differ from computed values by around 100 μV/K (Figure 6b). We explain this discrepancy by considering that α is more sensitive at low carrier concentrations, and Hg_2GeTe_4 possesses carrier concentration 2-4 orders of magnitude lower than that of $Cu_2HgGeTe_4$ (see Figure 6a). Similarly, the conductivity of $Cu_2HgGeTe_4$ is about 3 orders of magnitude above that of Hg_2GeTe_4, as shown in Fig S11.

Taking the value of the maximum measured α (Figure S6), the Goldsmid-Sharp band gap ($E_g = 2e|\alpha_{max}|T_{max}$)[37] for the ternary is calculated to be 0.40 eV, which matches closely with predicted DFT value from HSE06+SOC (0.48 eV). As discussed earlier, this is a larger band gap than that of $Cu_2HgGeTe_4$ (0.10 eV) due to the loss of Cu 3d orbital states. It is difficult to determine the Goldsmid-Sharp band gap for $Cu_2HgGeTe_4$ since this requires experimental α_{max}, which occurs at the rollover point when holes and electrons diffuse together. Due to the position of E_F inside of the valence band, this rollover will not occur, and a peak in temperature-dependent Seebeck is not be observed in our measurement temperature range of 323–523 K.

The Seebeck coefficient is a vital transport property in the experimental investigation of defects because it offers insight into both the Fermi energy (E_F) position and the density-of-states effective mass (m^*_{DOS}). Both can then also be compared to the corresponding parameters obtained in computation. The variation of Seebeck coefficient α and effective Fermi energy $E_{\mathrm{F}}^{\mathrm{eff}}$ is shown in Fig.6b, indicating the correlation of $E_{\mathrm{F}}^{\mathrm{eff}}$ to α. Experimentally, E_{F} is obtained by inputting the measured Seebeck coefficient and measured Hall carrier concentration at a given temperature (50°C) into a single parabolic band (SPB) model and assuming a scattering regime (Table S3).

SPB models generally are valid in regimes where bipolar conduction by minority electronic carriers is negligible. For $Cu_2HgGeTe_4$, the Fermi level is buried within the valence band and the degenerate carrier concentration is in excess of 10^{20} h^+ cm^{-3} across all invariant points for this compound (Fig S10). For Hg_2GeTe_4, the onset of minority carriers occurs around 160°C, indicated by the maximum in Seebeck coefficient (Fig S6). Carrier concentration is $\sim 10^{17}$ h^+ cm^{-3} and relatively invariant with temperature (Fig S10). Therefore we note that the SPB model is likely to break down for the ternary above this temperature. However it is valid at 50°C and permits analysis between the two compounds at this temperature.

Computationally, the position of E_{F} is obtained by solving for the charge neutrality condition in the quenched system at a certain measurement temperature (see Section 4.4). We note that this Fermi energy is an effective Fermi energy, since we assume that total defect concentrations are fixed at the synthesis temperature rather than equilibrated to the measurement temperature (while the relative concentrations of the different charge states of deep defects do equilibrate).

In Figure 6b, experimentally measured and computationally predicted E_{F} are plotted. E_{F} is referenced to the VBM, i.e. a positive value indicates that E_{F} is above the VBM or inside the gap (as is the case for both doped and undoped Hg_2GeTe_4) and a negative value means that E_{F} is inside the valence band ($Cu_2HgGeTe_4$). Comparison of experimental and computational α and E_{F} helps validate the defect calculations. For example, as we walk the path from A to F^0 (left to right in Figure 6b), we observe a trend of overall increasing α and increasing E_{F}. The matching trend between E_{F} and Seebeck coefficient helps validate our defect calculations, since Seebeck is a measure of the position of E_{F}. We can link the increasing E_{F} back to the removal of Cu-related defects along this chemical potential path, which permits the E_{F} to lift out of the valence band and away from the band edge, which permits a greater Seebeck coefficient.

Looking more closely at the comparison of experimental (blue x's) and computational (blue lines) E_{F}, we find that they are in very good agreement for the ternary, with both positioning E_{F} in close proximity to the VBM. For the quaternary, both theory and experiment predict a negative value of E_{F}, confirming our understanding of E_{F} as buried within the valence band of $Cu_2HgGeTe_4$ (degenerate p-type). The experimentally estimated E_{F} lies significantly deeper, however, than the predicted values, likely due to the sensitivity of our SPB model when α is very small. For example, Sample A and B have small Seebeck coefficients of 31.0 and 9.3 μV/K, respectively, (50°C) and the estimated E_{F} of Sample B is over three times (nearly 1.5 eV deeper into the VB) than Sample A. Sample B deviates the most from predicted E_{F}, which is also the point where computationally we predict the highest carrier concentration (most metallic behavior and lowest Seebeck). In contrast, the ternary samples each possess α greater than 300μV/K and while their specific values range from 312 (Sample D^0) to 383 μV/K (Sample E^0), their E_{F} are very close and differ by only 0.03 eV.

The density of states effective mass (m^*_{DOS}) estimated from experimental data using our SPB model is found to be larger for the quaternary ($m^*_{\mathrm{DOS}} = 0.49\ m_e$) than the ternary compound ($m^*_{\mathrm{DOS}} = 0.21\ m_e$). These values also match well with computational predictions: for $Cu_2HgGeTe_4$ samples, the electronic structure calculation yields $m^*_{\mathrm{DOS}} = 0.50\ m_e$ (valence band), while for the Hg_2GeTe_4 it yields $m^*_{\mathrm{DOS}} = 0.32\ m_e$ (valence band) (Figure S8). We note a few caveats with the experimental determination of these parameters, related to the need to select a scattering regime for the SPB model. Ionized impurity scattering is assumed to be the dominant scattering type for the ternary (scattering parameter $r = 1.5$)[38] due to the measured increase in mobility with temperature (Figure S7). For the quaternary, a combination of ionized impurity scattering and acoustic phonon scattering (r = -0.5)[38] is assumed since the mobility shows a very weak temperature dependence. We crudely assert a scattering parameter of r = 1 for the quaternary to account for both mechanisms (Figure S7). These dominant scattering types are corroborated by computations from AMSET (Figure S5).

2.3.3 n-type dopability limit

Using semi-empirical modeling for the quality factor (β)[18], which is a measure of the optimized zT for bulk materials, we have assessed the p- and n-type TE potential for $Cu_2HgGeTe_4$ and Hg_2GeTe_4 (Supplementary Information section 5). It is shown that both compounds have better n-type TE performance than PbTe (1.2 times higher for Hg_2GeTe_4 and 3.8 times higher for $Cu_2HgGeTe_4$) if the electron concentration is optimized. However, the p-type TE performance is moderate, just like many other well-known DLS phases, even when doped to the optimized carrier concentrations. Therefore, we focus on the possibility of achieving majority n-type carriers in both compounds.

We consider the *ideal n-type dopability*, i.e. the maximum achievable n-type carrier concentration as the elemental chemical potentials are varied. This is shown in Figure 6c which displays the maximum n-type carrier concentration (and the corresponding hole population) along the Brouwer diagram chemical potential path. The ideal dopability is calculated by assuming an ideal extrinsic dopant that drives the Fermi energy to the position where the lowest energy compensating acceptor defect has zero $\Delta E_{D,q}$. While practically identifying such an ideal dopant is often impossible, the ideal dopability sets an upper bound to the carrier concentrations achievable.

As expected, Figure 6c shows that $Cu_2HgGeTe_4$ (A to F) is always p-type, even when doped by an optimal n-type dopant. This behavior is driven by the low energy native Cu_{Hg} and V_{Cu} defects. In the limit of ideal n-type doping, the hole carrier concentration still ranges between 10^{18}-10^{22} cm^{-3}. Similarly, for Cu-doped Hg_2GeTe_4 (D' to F'), holes are always the majority carriers due to the presence of Cu_{Hg} defects (Figure 5b), with hole carrier concentrations ranging between 10^{16}-10^{17} cm^{-3}. For these two cases, achieving majority *n*-type conduction is not possible.

By contrast, for Cu-free Hg_2GeTe_4 we observe that achieving majority *n*-type carriers is possible with carrier concentrations approaching up to $\sim10^{18}$ cm^{-3}. At all points plotted, the maximum *n*-type carrier concentration is limited by V_{Hg} counter-defect. The maximum dopability occurs when E_F reaches the point where V_{Hg} has zero $\Delta E_{D,q}$. At F^0, the most favorable point for *n*-type doping, ideal doping corresponds approximately to E_F around 0.07 eV above the conduction band edge in Figure 4c. For the other points in the Brouwer diagram, the formation energy of V_{Hg} goes to zero inside the band gap. It is of note that even at optimal point F^0, despite that E_F is above the conduction band edge, the electron carrier concentration reaches only 7.9×10^{17} cm^{-3}. The relatively low carrier concentration arises from the exceptionally small conduction band DOS effective mass ($m^*_{DOS,CB}$ = 0.02 m_e) and low conduction band degeneracy (N_v^{CB} = 1) for Hg_2GeTe_4. Therefore, while n-type doping appears to be possible in HGT, this finding highlights some additional challenges in achieving high carrier concentrations. Namely, in addition to pinning E_F close or inside the band, a material with favorable electronic structure with high m^*_{DOS} and high N_v will better facilitate extrinsic doping.

3 Conclusion

In this work, we studied the defect chemistry of two diamond-like semiconductors, $Cu_2HgGeTe_4$ and Hg_2GeTe_4, using first-principles calculations and experiment. We found interesting reciprocal challenges in doping for $Cu_2HgGeTe_4$ and Hg_2GeTe_4. The stability region for $Cu_2HgGeTe_4$ and Hg_2GeTe_4 is visualized in both two-dimensional and three-dimensional chemical potential space. Defect calculations are then coupled with an understanding of thermodynamic stability to reveal the difference in defect chemistry. The quaternary $Cu_2HgGeTe_4$, with a wide range of tunable chemical potentials, is degenerate *p*-type at all growth conditions due to an abundance of limiting defects: Cu_{Hg} at Cu-rich cases and V_{Cu} at Cu-poor conditions, therefore resisting extrinsic *n*-type doping. On the other hand, the ternary Hg_2GeTe_4, which has a narrow stability window, exhibits intrinsic behavior with a bi-polar dopability window. A Brouwer band diagram approach is utilized to visualize the role of native defects on carrier concentrations, dopability, and transport properties. Using phase boundary mapping, carrier concentrations are predicted from self-consistent defect calculations and compared to measured experimental carrier concentrations, generally showing good agreement.

The understanding of native defect chemistry in $Cu_2HgGeTe_4$ and Hg_2GeTe_4 not only provides guidelines for manipulating intrinsic defects to optimize the carrier concentrations in these two materials, but also gives general insights into design strategies to identify DLS materials with larger dopability windows. Although $Cu_2HgGeTe_4$ has good predicted *n*-type TE performance, the combination of V_{Cu} and Cu_{Hg} defects limits the accessible Fermi energy range and prohibits n-type doping. Meanwhile, the Cu-free analogue, ordered vacancy compound $HgGeTe_4$, shows a dopability window and the possibility of achieving majority n-type carriers. The two materials show a correspondence in their native defect chemistry, such that these differences in dopability largely arise from the absence of Cu-related defects in the ternary and its different band edge positions. We suggest that the family of ordered-vacancy compounds related to quaternary DLS therefore may contain dopable TE candidate materials. These results shed light on how native defects and their manipulation can enable (and sometimes even limit) design of dopable diamond like semiconductors.

4 Methods

4.1 Structural Relaxation

Density functional theory (DFT) calculations were performed with the Vienna ab initio Simulation Package (VASP)[39] using Projector Augmented Wave (PAW)[40] pseudopotentials. The Heyd-Scuseria-Ernzerhof[41] (HSE06) hybrid exchange correlation functional was used with an exchange mixing of α = 0.25. A plane-wave energy cutoff of 400 eV and a 4×4×4 Monkhorst-Pack *k*-point sampling was used to relax the structures to give converged total energies. The total energy and force convergence criteria used in this study was 10^{-5} eV and 0.02 eV/Å, respectively.

4.2 Phase stability analysis

The thermodynamic stability of $Cu_2HgGeTe_4$ and Hg_2GeTe_4 against decomposition into secondary phases was determined using the convex hull analysis. The secondary phases (unary, binary, ternary and quaternary) considered were from the Inorganic Crystal Structure Database[42] (ICSD). The total energies of the secondary phases were calculated by relaxing the structure following the same procedure as described above. The elemental chemical potential is obtained by bulk relaxation using HSE06, which has been shown to provide accurate predictions of formation enthalpies compared with experiments.[43]

The phase stability region in chemical potential space is thermodynamically limited by several conditions, including avoiding precipitation of host element phases, avoiding the formation of secondary phases composed of the host elements and maintaining thermodynamic equilibrium of the main compound. For quaternary $Cu_2HgGeTe_4$, the stability region is restricted to several four-phase corners of the polyhedron in Figure 2: at each corner $Cu_2HgGeTe_4$ is in equilibrium with 3 other secondary phases, while for Hg_2GeTe_4 the corners are three-phase equilibrium.

4.3 Native Defect Energetics

To understand the native defect chemistry, we employ the standard supercell approach[44] to calculate defect formation energies of native point defects. The defect formation energy ($\Delta E_{D,q}$) is calculated from the total energies as follows:

$$\Delta E_{D,q} = E_{D,q} - E_{host} + \sum_i n_i \mu_i + qE_F + E_{corr} \tag{1}$$

where $\Delta E_{D,q}$ represents the formation energy of a defect D in charge state q; $E_{D,q}$ and E_H are the total energies of the supercell with and without the defects, respectively; μ_i is the atomic chemical potential of elemental species i added ($n_i < 0$) or removed ($n_i > 0$) from the host supercell to form defects; E_F is the Fermi energy, which varies from the valence band maximum (VBM) to the conduction band minimum (CBM). Finally, E_{corr} is the term that accounts for the finite-size corrections within the supercell approach. From Equation. 1, we can understand that the defect formation energy depends on elemental chemical potentials, which are thermodynamically limited by several conditions (see Section 4.2).

For the defect calculations, we built supercells for $Cu_2HgGeTe_4$ and Hg_2GeTe_4 with 64 and 56 atoms, respectively, and fully relaxed the structures in HSE06 to obtain the total energies. The Brillouin zone sampling with Γ-centered $2 \times 2 \times 2$ k-point grid was used to relax the supercells. The following corrections to the defect formation energies ($\Delta E_{D,q}$) were included as described by Lany and Zunger[44]: (1) image charge correction for charged defects, (2) potential alignment correction for charged defects, and (3) band gap correction. The static dielectric constant (electronic + ionic) needed for image-charge corrections are evaluated using density functional perturbation theory (DFPT) as implemented in VASP.[39]

Spin-orbit coupling (SOC) effects were taken into consideration for $Cu_2HgGeTe_4$ and Hg_2GeTe_4 due to the presence of heavy elements Hg and Te. The band gap calculated by HSE06 was corrected by applying band edge shifts determined by comparing the average electrostatic potential to match calculations from HSE06+SOC (Figure S2). The band gaps in the defect diagrams are the corrected gaps from HSE06+SOC calculations.

The native point defects considered include vacancies (V_{Cu}, V_{Hg}, V_{Ge}, V_{Te}), antisite defects (Cu_{Hg}, Hg_{Cu}, Ge_{Hg}, Hg_{Ge}) and interstitial defects (Cu_i, Hg_i). The interstitial defects are at tetrahedral sites for Cu_i and Hg_i (Figure S9). The interstitial defects for Ge_i and Te_i are not considered in this work due to the large ionic radius which will make defects energetically unfavorable. All unique Wyckoff positions (see Figure 1) were considered in the calculations for vacancies, interstitial and antisite defects. A python toolkit for visualizing phase stability and defect chemistry, VTAnDeM (github.com/ertekin-research-group/VTAnDeM)[45], is used in this work for creating phase diagrams and defect diagrams.

4.4 Defect and Carrier Concentrations

The free carrier concentrations at specific temperatures were calculated by solving the charge-neutrality condition. The charge neutrality condition is given as:

$$\sum_{D} qC_{D,q} - n + p = 0 \tag{2}$$

where q is the charge state of the defects, and n and p are the free electron and hole concentrations, respectively. The concentration of a defect can be obtained by:

$$C_{D,q} = N exp\left(\frac{-\Delta E_{D,q}}{k_B T}\right) \tag{3}$$

where N is the concentration of the corresponding lattice sites, k_B is the Boltzman constant and $\Delta E_{D,q}$ is the defect formation energy. This relation is valid at thermodynamic equilibrium and in the dilute regime where the defect concentration is sufficiently low such that defect-defect interactions are negligible.

The carrier concentration can then be analytically approximated as:

$$n \approx 2\left[\frac{2\pi m_e^* k_B T}{h^2}\right]^{3/2} \exp\left(\frac{E_F - E_{CBM}}{k_B T}\right) \tag{4}$$

$$p \approx 2\left[\frac{2\pi m_h^* k_B T}{h^2}\right]^{3/2} \exp\left(\frac{E_{VBM} - E_F}{k_B T}\right) \tag{5}$$

where m_e^* and m_h^* are the density-of-states (DOS) effective masses for electrons and holes, respectively. The DOS effective mass (m_{DOS}^*) is extracted from a 100 meV energy window away from the band edge positions under a parabolic band approximation.

When solving for the charge neutrality condition, we assume a 'quench' scenario, where the total concentration of a given defect (including all charge states) is fixed to the concentration generated at the synthesis temperature while different charge states of the defect can thermally equilibrate with each other according to the thermodynamic partition function. That is, we allow carrier exchange between defects and the valence and conduction bands. When a material is quenched to the measurement temperatures, free carriers and the ionization level of each type of defect will re-equilibrate to satisfy the charge neutrality condition, with the corresponding Fermi energy satisfying charge neutrality being an effective Fermi energy (E_F^{eff}).

4.5 Electrical transport properties

The *ab initio* scattering and transport (AMSET)[35] software package is used to calculate the electron lifetimes and transport properties. All *ab initio* inputs (dielectric constant, elastic constant, deformation potential, polar optical phonon frequencies) are computed from density functional theory (DFT) using the HSE06 exchange-correlation functional, except electronic structures which are calculated using HSE06 together with SOC. The calculated materials parameters used to compute scattering rates, including elastic constants, dielectric tensors, deformation potentials and phonon frequency are summarized in Table S2. We use the corrected band gap as explained in Section 4.3. Using band energies from HSE06+SOC electronic structure calculations as input, the Seebeck coefficients are calculated from the Onsager transport coefficients. A dense interpolated k-point mesh of 39×39×47 in the Brillouin zone was adopted for converged results.

4.6 Synthesis

Pellet samples of the quaternary ($Cu_2HgGeTe_4$) from a previous study[15] were used here. To verify that no oxidation or deleterious sample evolution occurred during storage, a full suite of electronic measurements from 298 K to 523 K were performed for each sample and checked against original measurements. Ternary

(Hg_2GeTe_4) samples were synthesized for this study, according to the following procedure. Appropriate ratios of high purity Hg (liquid, Alfa 99.999%), Ge (ingot, Indium Corp, 99.999%, and Te (ingot, 5NPlus Inc. 99.999%) were weighed in batches totaling 10 g of material and loaded into tungsten carbide ball mill vials. The samples underwent 90 minutes of ball milling in a nitrogen dry box with oxygen levels under 1 ppm. The resulting powders were ground with an agate mortar and pestle, passed through a 200-mesh sieve, and loaded into clean fused silica ampoules. The ampoules were then sealed under vacuum and annealed at 623 K for 72 hours. After annealing treatment, the ampoules were returned to the inert glovebox environment, where they were broken to extract the consolidated ingots. Grinding and sieving were repeated, and approximately 3 g of powder from each sample were loaded into graphite dies for hot pressing. Samples underwent uniaxial hot pressing at 623 K under 40 MPa for 6 hours, followed by 1 hour of pressureless annealing. Final pellets were passively cooled to room temperature, removed from graphite dies, and polished to a parallelness of ± 5 μm in preparation for measurements.

4.7 Measurement

A combination of X-ray diffraction (XRD), scanning electron microscopy (SEM), and energy dispersive spectroscopy (EDS) was performed on each sample to confirm its phase content. The XRD data were collected on a Bruker D2 Phaser diffractometer in θ-2θ mode from 10 to 80° of 2θ and diffraction patterns of each sample were compared against data from ICSD 759707 (Hg_2GeTe_4). SEM and EDS were performed on a FEI Quanta 600i SEM. Measurement of the Seebeck coefficient was performed at 323 K using a custom-built apparatus[36] Hall effect measurements were taken on a custom built apparatus with Van der Pauw geometry from 323 K to 473 K.[46] All samples underwent at least two heating and cooling cycles to rule out possible sample evolution during measurement or annealing to instrument contacts.

Conflicts of Interest

There are no conflicts of interest to declare.

Acknowledgements

This work was funded primarily with support from the U.S. ational Science Foundation (NSF) via Grant No. DMR1729149. J.Q. acknowledges funding from NSF DIGI-MAT program, Grant No. 1922758. M.Y.T. is funded by the United States Department of Energy through the Computational Science Graduate Fellowship (DOE CSGF) under Grant No. DE-SC0020347. J. Q. and C. E. P acknowledge helpful discussions with Prashun Gorai and Kamil Ciesielski.

References

1 J. Yoon, S. Jo, I. S. Chun, I. Jung, H.-S. Kim, M. Meitl, E. Menard, X. Li, J. J. Coleman, U. Paik *et al.*, *Nature*, 2010, **465**, 329–333.
2 P. Yu, C.-H. Chang, C.-H. Chiu, C.-S. Yang, J.-C. Yu, H.-C. Kuo, S.-H. Hsu and Y.-C. Chang, *Advanced materials*, 2009, **21**, 1618–1621.
3 J. Lee, J. Wu, M. Shi, J. Yoon, S.-I. Park, M. Li, Z. Liu, Y. Huang and J. A. Rogers, *Advanced Materials*, 2011, **23**, 986–991.
4 S.-H. Wei and S. Zhang, *Journal of Physics and Chemistry of solids*, 2005, **66**, 1994–1999.
5 M. G. Panthani, V. Akhavan, B. Goodfellow, J. P. Schmidtke, L. Dunn, A. Dodabalapur, P. F. Barbara and B. A. Korgel, *Journal of the American Chemical Society*, 2008, **130**, 16770–16777.
6 A. E. Delahoy, L. Chen, M. Akhtar, B. Sang and S. Guo, *Solar energy*, 2004, **77**, 785–793.
7 S. C. Riha, B. A. Parkinson and A. L. Prieto, *Journal of the American Chemical Society*, 2009, **131**, 12054–12055.
8 H. Katagiri, K. Jimbo, W. S. Maw, K. Oishi, M. Yamazaki, H. Araki and A. Takeuchi, *Thin Solid Films*, 2009, **517**, 2455–2460.
9 S. Chen, A. Walsh, X.-G. Gong and S.-H. Wei, *Advanced materials*, 2013, **25**, 1522–1539.
10 B. R. Ortiz, W. Peng, L. C. Gomes, P. Gorai, T. Zhu, D. M. Smiadak, G. J. Snyder, V. Stevanović, E. Ertekin, A. Zevalkink *et al.*, *Chemistry of Materials*, 2018, **30**, 3395–3409.
11 Y. Luo, J. Yang, Q. Jiang, W. Li, D. Zhang, Z. Zhou, Y. Cheng, Y. Ren and X. He, *Advanced Energy Materials*, 2016, **6**, 1600007.
12 W. D. Carr and D. T. Morelli, *Journal of Alloys and Compounds*, 2015, **630**, 277–281.
13 R. Liu, L. Xi, H. Liu, X. Shi, W. Zhang and L. Chen, *Chemical Communications*, 2012, **48**, 3818–3820.
14 T. Plirdpring, K. Kurosaki, A. Kosuga, T. Day, S. Firdosy, V. Ravi, G. J. Snyder, A. Harnwunggmoung, T. Sugahara, Y. Ohishi *et al.*, *Advanced Materials*, 2012, **24**, 3622–3626.
15 B. R. Ortiz, K. Gordiz, L. C. Gomes, T. Braden, J. M. Adamczyk, J. Qu, E. Ertekin and E. S. Toberer, *Journal of materials chemistry A*, 2019, **7**, 621–631.
16 A. Belsky, M. Hellenbrandt, V. L. Karen and P. Luksch, *Acta Crystallogr. B*, 2002, **58**, 364.
17 E. J. Skoug and D. T. Morelli, *Physical review letters*, 2011, **107**, 235901.
18 J. Yan, P. Gorai, B. Ortiz, S. Miller, S. A. Barnett, T. Mason, V. Stevanović and E. S. Toberer, *Energy Environ. Sci.*, 2015, **8**, 983–994.
19 J. M. Adamczyk, L. C. Gomes, J. Qu, G. A. Rome, S. M. Baumann, E. Ertekin and E. S. Toberer, *Chemistry of Materials*, 2020.
20 S. A. Miller, M. Dylla, S. Anand, K. Gordiz, G. J. Snyder and E. S. Toberer, *npj Computational Materials*, 2018, **4**, 1–8.
21 S. Chen, J.-H. Yang, X.-G. Gong, A. Walsh and S.-H. Wei, *Physical Review B*, 2010, **81**, 245204.
22 S. Chen, A. Walsh, X.-G. Gong and S.-H. Wei, *Advanced materials*, 2013, **25**, 1522–1539.
23 B. L. Levy-Wendt, B. R. Ortiz, L. C. Gomes, K. H. Stone, D. Passarello, E. Ertekin, E. S. Toberer, M. F. Toney, D. Collaboration

et al., *Physical Review Materials*, 2021, **5**, 015402.

24 S. Ohno, K. Imasato, S. Anand, H. Tamaki, S. D. Kang, P. Gorai, H. K. Sato, E. S. Toberer, T. Kanno and G. J. Snyder, *Joule*, 2018, **2**, 141.

25 S. Nakamura, T. Maeda and T. Wada, *Japanese Journal of Applied Physics*, 2010, **49**, 121203.

26 S. Chen, X. Gong, A. Walsh and S.-H. Wei, *Applied Physics Letters*, 2009, **94**, 041903.

27 S. Chen, A. Walsh, Y. Luo, J.-H. Yang, X. Gong and S.-H. Wei, *Physical Review B*, 2010, **82**, 195203.

28 N. Kim, P. P. Martin, A. A. Rockett and E. Ertekin, *IEEE Journal of Photovoltaics*, 2017, **7**, 1781–1788.

29 S. Zhang, S.-H. Wei, A. Zunger and H. Katayama-Yoshida, *Physical Review B*, 1998, **57**, 9642.

30 C. Persson, Y.-J. Zhao, S. Lany and A. Zunger, *Physical Review B*, 2005, **72**, 035211.

31 J. Pohl and K. Albe, *Journal of Applied Physics*, 2010, **108**, 023509.

32 M. Toriyama, J. Qu, G. J. Snyder and P. Gorai, *ChemRxiv*, 2021.

33 D. T. Do and S. Mahanti, *Journal of Alloys and Compounds*, 2015, **625**, 346–354.

34 D. T. Do and S. D. Mahanti, *Journal of Physics and Chemistry of Solids*, 2014, **75**, 477–485.

35 A. M. Ganose, J. Park, A. Faghaninia, R. Woods-Robinson, K. A. Persson and A. Jain, *Nature Communications*, 2021, **12**, 1–9.

36 S. Iwanaga, E. S. Toberer, A. LaLonde and G. J. Snyder, *Review of Scientific Instruments*, 2011, **82**, 063905.

37 Z. M. Gibbs, H.-S. Kim, H. Wang and G. J. Snyder, *Applied Physics Letters*, 2015, **106**, 022112.

38 K. Ahn, C.-P. Li, C. Uher and M. G. Kanatzidis, *Chemistry of Materials*, 2010, **22**, 876–882.

39 G. Kresse and J. Furthmüller, *Phys. Rev. B*, 1996, **54**, 11169–11186.

40 P. E. Blöchl, *Phys. Rev. B*, 1994, **50**, 17953–17979.

41 A. V. Krukau, O. A. Vydrov, A. F. Izmaylov and G. E. Scuseria, *The Journal of chemical physics*, 2006, **125**, 224106.

42 A. Belsky, M. Hellenbrandt, V. L. Karen and P. Luksch, *Acta Crystallogr. B*, 2002, **58**, 364.

43 N. Kim, P. P. Martin, A. A. Rockett and E. Ertekin, *Physical Review B*, 2016, **93**, 165202.

44 S. Lany and A. Zunger, *Phys. Rev. B*, 2008, **78**, 235104.

45 *The Visualization Toolkit for Analyzing Defects in Materials (VTAnDeM)*, `https://https://github.com/ertekin-research-group/VTAnDeM`.

46 K. A. Borup, E. S. Toberer, L. D. Zoltan, G. Nakatsukasa, M. Errico, J.-P. Fleurial, B. B. Iversen and G. J. Snyder, *Review of Scientific Instruments*, 2012, **83**, 123902.